The Astrophysical Journal, 979:207 (13pp), 2025 February 1 https://doi.org/10.3847/1538-4357/ada1d6

Dynamics and Energetics of Resistive, Thermally Conductive, and Radiative Plasma in Coronal Current Sheets due to Asymmetric External Perturbation

Sripan Mondal, Akash Bairagi, and A. K. Srivastava
Department of Physics, Indian Institute of Technology (BHU), Varanasi-221005, India; sripanmondal.rs.phy21@itbhu.ac.in, asrivastava.app@itbhu.ac.in
Received 2024 November 18; revised 2024 December 10; accepted 2024 December 15; published 2025 January 28

Abstract

We study the asymmetric interaction of wave-like velocity perturbation with a coronal current sheet (CS) in the presence of resistivity, thermal conduction (TC), and radiative cooling (RC). We analyze the dynamics and energetics of the CS in four cases, namely, (i) no energy loss, (ii) TC only, (iii) RC only, and (iv) TC+RC. Before fragmentation, thinning and elongation of the CS are found to be identical in all four cases and therefore independent of the presence or absence of energy loss effects. Onset times, corresponding Lundquist numbers, and aspect ratios suggest that TC advances the onset of fragmentation while RC has the opposite effect in comparison to the absence of energy losses. Reconnection takes place at a higher rate in the presence of TC and TC+RC in the tearing unstable CS. Speeds of plasmoids are also found to be higher under the effect of TC and TC+RC. In the presence of TC and TC+RC, average density becomes higher within the tearing unstable CS than in the other two cases. As expected, the estimated average temperature is increasing with the highest and lowest rates in the absence of energy losses and in the presence of both TC and RC, respectively. After the onset of fragmentation, the rate of decrement of average magnetic energy density and increment of average kinetic energy density becomes higher in the presence of TC and TC+RC than in the other two cases. Thus, we conclude that the presence of energy-loss mechanisms critically influences the dynamics, energetics, and plasmoid formation within a reconnecting coronal CS.

Unified Astronomy Thesaurus concepts: Solar magnetic reconnection (1504)

Materials only available in the online version of record: animation

1. Introduction

Magnetic reconnection forms the basis of the generation of kinetic energy of charged particles in plasma and thermalizes it by the liberation of the stored magnetic energy. In addition, magnetic reconnection is an essential mechanism for triggering solar eruptions such as solar flares and coronal mass ejections (CMEs). The occurrence of this process is not limited to the solar atmosphere only, as it eventually occurs in the laboratory, in space, and in magnetospheric and astrophysical plasma systems at diverse spatiotemporal scales (E. Priest 2014; R. A. Treumann & W. Baumjohann 2015; D. I. Pontin & E. R. Priest 2022). Reconnection is basically a three-dimensional process that can take place at locations of high gradient of magnetic field such as magnetic nulls, separators, separatrix surfaces, quasi-separators or hyperbolic flux tubes, and bald patches (E. Priest 2014; D. I. Pontin & E. R. Priest 2022). More importantly, irrespective of the initial magnetic geometry, formation of the current sheet (CS) is essential for onset of the magnetic reconnection. However, the CS can either remain stable or act as a host of the magnetic reconnection. Either current-dependent enhanced resistivity related to the magnetohydrodynamic turbulences (K. Shibata & S. Tanuma 2001) or external perturbations in the form of EUV waves or shock waves (G. Vekstein 2017; S. Mondal et al. 2024a) can perturb the CS. As a result of such perturbations, the magnetic fields start to reconnect or slip through each other within the CS and cause several topological changes (see E. Priest 2014; D. I. Pontin & E. R. Priest 2022 and references therein for more details).

Even though externally driven or forced reconnection has been studied theoretically for a long time (J. Sakai et al. 1984; D. Odstrcil & M. Karlicky 1997), A. K. Srivastava et al. (2019) presented the first direct imaging of the forced magnetic reconnection at a considerably high rate at a temporary X-point in the solar corona as seen by Solar Dynamics Observatory (SDO)/Atmospheric Imaging Assembly (AIA; J. R. Lemen et al. 2012), where the CS has been formed owing to plasma inflows created by a prominence eruption. Subsequently in the follow-up observations by SDO/AIA, A. K. Srivastava et al. (2021) studied extensively the forced magnetic reconnection that is creating the jetlike features and hot plasma flows in the off-limb corona. G. Zhou et al. (2020) have reported that the interaction of a magnetic null with shock waves results in its 40 minute oscillation and further occurrence of magnetic reconnection there within a coronal loop system, connecting active regions (ARs) AR 11429 and AR 11430. Now, plasma sheets, i.e., apparent CSs of diverse lengths and widths, are ubiquitous during flares, eruptions, and jets (R. Liu et al. 2010; X. Cheng et al. 2018; Y. Li et al. 2018; R. Patel et al. 2020; T. Ding & J. Zhang 2024; L. Yang et al. 2024). Likewise, the generation and propagation of large-scale EUV waves are also reported in several observational studies (N. V. Nitta et al. 2013; W. Liu & L. Ofman 2014; N. Muhr et al. 2014; K. Vanninathan et al. 2015; D. M. Long et al. 2017; Y. Shen et al. 2018; A. M. Veronig et al. 2018; G. Mann & A. M. Veronig 2023). Hence, in principle, both CSs and EUV waves can interact with each other in the solar corona.

Although there have been no direct coronal observations specifically focusing on the interaction of EUV waves and the

CS until now, recently P. Kumar et al. (2024) provided observational evidence of the mode conversion of a fast MHD wave during its interaction with a 3D magnetic null. Symbiosis of waves and reconnection in the formed CS may play an important role in augmenting existing knowledge about the long-standing coronal heating problem (S. Mondal et al. 2024b; A. K. Srivastava et al. 2024). However, their observational baseline should act to further support the physical models and their exclusive physical scenario. Moreover, there are observations of flares or eruptions initiated via shock waves or EUV waves that originated during another distant earlier flare or eruption (e.g., Z. Svestka 1981; F. Fárnìk et al. 1983; H. Wang et al. 2001). Therefore, such spatiotemporally correlated sympathetic events may serve as a spatially unresolved potential indirect signature of magnetic reconnection initiated via the interaction of EUV or shock waves with a magnetic null or CS. Moreover, in other plasma systems, such as in Earth's magnetosphere, it has been reported that the non-reconnecting CS got compressed owing to its interaction with a bow shock near magnetopause in the magnetosheath, which can result in the onset of magnetic reconnection within that CS (N. C. Maynard et al. 2007; J. A. Kropotina et al. 2021). Therefore, more focused observations on this particular aspect of the interaction of EUV waves or fast shock waves and non-reconnecting quasi-stable CSs may provide some direct signature of such an interaction also in the solar corona in the future.

Most of the large-scale impulsive eruptions, such as flares, CMEs, and filaments, are attributed to the fast reconnection. Fragmentation of an elongated and narrow CS and subsequent plasmoid formation via tearing mode instability have been extensively studied for decades as one of the mechanisms to achieve a high reconnection rate theoretically (N. F. Loureiro et al. 2007; A. Bhattacharjee et al. 2009; Y.-M. Huang & A. Bhattacharjee 2010, 2016; L. Comisso et al. 2017). High-resolution observational facilities further confirm the presence of these fragmented structures and dense plasma blobs within elongated narrow intensity features, i.e., CSs or even in jets (P. Riley et al. 2007; L.-J. Guo et al. 2013; R.-Y. Kwon et al. 2016; Q. M. Zhang et al. 2016; J. Chae et al. 2017; X. Cheng et al. 2018; R. J. French et al. 2020; R. Patel et al. 2020; R. J. French et al. 2021). Although the tearing instability has been studied extensively in the solar corona, there are only a few studies where this tearing mode has been achieved without any localized enhancement of resistivity (H. Baty et al. 2009; T. Shimizu & K. Kondoh 2022; Ø. H. Færder et al. 2024). In addition, the role of various energy-loss mechanisms, such as thermal conduction (TC) and radiative cooling (RC), in CS dynamics and associated magnetic reconnection is not explored in greater detail. Even though both TC and RC are energy-loss processes, the basic mechanisms are different, such as (i) TC depends on the temperature gradient, i.e., it conducts heat from high-temperature regions to relatively cooler regions, whereas (ii) RC is directly connected to the density of the emitter and also to a temperature-dependent cooling function. Therefore, it is important to explore their individual and resultant effects on the dynamical and, more importantly, thermal characteristics related to the magnetic reconnection. The observable apparent CSs are unique in the solar corona, which manifests the evolution of temperature, density, and plasma flows in them distinctly (T. Ding & J. Zhang 2024). This is most likely attributed to the different roles of the thermodynamical properties set within them.

L. Ledentsov (2021a, 2021b) reported that the presence of nonadiabatic effects such as radiative loss and TC can modify the growth rate of tearing instability in the linear regime. S. Sen & R. Keppens (2022) explored the role of radiative loss and background heating on tearing instability in a CS via a 2D resistive MHD simulation. They found that the explosive nature of reconnection is more achievable at a relatively lower Lundquist number owing to the positive feedback between tearing and thermal instabilities caused by the presence of radiative loss. However, they used magnetic field perturbations to achieve the magnetic reconnection in the absence of TC, which is an effective energy-loss effect in the solar corona. In addition, they did not consider the presence of the guide field that is omnipresent in the solar corona, especially in ARs, and can suppress plasmoid formation. S. Mondal et al. (2024a) studied the external forcing aspect in the form of velocity perturbation for the onset of reconnection and subsequent plasmoid formation in the absence of any kind of energy-loss effects. The absence of any energy-loss mechanism results in a temperature enhancement up to 20 MK at the core of plasmoids. Hence, it is interesting to see the effects of energy-loss mechanisms on the temperature of plasmoids and the associated CSs, as well as how these candidates influence the physical processes and morphological appearance overall. In addition, it is of utmost importance to check the temporal evolution of different forms of energy, such as magnetic energy and kinetic energy, for different cases, i.e., without any energy-loss effects, with TC only, with RC only, and in the presence of both TC and RC.

In this paper, following S. Mondal et al. (2024a), we impose an external forcing, but in a new form of anisotropically propagating velocity pulse for perturbing the model CS in the presence of TC and RC. We explore the evolution of different forms of energies with time in the aforementioned different cases and make possible physics-wise interpretations. In Section 2, we describe the numerical setup and methods. In Section 3, we report the results. In Section 4, we summarize the results and compare them with previous studies, and we discuss their possible physical implications.

2. Numerical Setup and Methods

We perform a 2.5D magnetohydrodynamic simulation to study the onset and evolution of the magnetic reconnection and associated energetics in a force-free Harris CS as given by (C. Xia et al. 2018; S. Mondal et al. 2024a)

$$B_x = 0 \tag{1}$$

$$B_y = -B_0 \tanh\left(\frac{x}{l}\right) \tag{2}$$

$$B_z = B_0 \,\mathrm{sech}\left(\frac{x}{l}\right), \tag{3}$$

where B_x and B_y are the magnetic field components in the plane in which entire dynamical and energetic processes of the CS are captured. The nonzero B_z component ensures that a vanishing Lorentz force maintains the unstratified homogeneous corona in magnetohydrostatic equilibrium initially in the presence of uniform plasma pressure. Basically, we use the same initial magnetic field configuration as described in

S. Mondal et al. (2024a), i.e., the magnetic field amplitude (B_0) and CS half-width (l) are 10 G and 1.5 Mm, respectively. Following S. Mondal et al. (2024a), the uniform temperature and density are taken to be 1 MK and 2.34×10^{-15} g cm^{-3}, respectively, with a plasma β of 0.079 to ensure typical coronal conditions. Basically, S. Mondal et al. (2024a) studied the onset of magnetic reconnection and tearing mode instability and subsequent multiple stages of plasmoid formations in detail when the CS has been perturbed symmetrically at the center of its length by an isotropically propagating velocity pulse. But in reality, it is more likely that any perturbation will be anisotropic and that it can interact with the CS at any point along its length. In addition, it is interesting to consider energy-loss mechanisms such as field-aligned TC and RC to study their individual and collective effects on all the physical processes and dynamics of the CS.

Since we are studying the dynamics in a 2.5D space, physical variables should not possess any z-dependence, i.e., any perturbation also must be a function of x and y only. So, we perturb the initial equilibrium with a force-free stable CS via imposing an anisotropically propagating Gaussian pulse given by (S. Mondal et al. 2024b)

$$v_x = v_0 \quad \exp\left(-\left(\frac{x - x_0}{w_x}\right)^2 - \left(\frac{y - y_0}{w_y}\right)^2\right). \tag{4}$$

Here x_0 is set at 15 Mm left from the center of the CS at $x = 0$, and y_0 is set at a height of 65 Mm. Therefore, the perturbation will interact with the CS at $y = 65$ Mm with the highest amplitude due to lowest distance between its epicenter and the CS. This further confirms an interaction that is asymmetric about the length of the CS. The widths of this Gaussian pulse in x- and y-direction, i.e., w_x and w_y are taken to be 6 Mm and 2 Mm respectively. The amplitude (v_0) of the velocity pulse is 350 km s^{-1} that is $0.6\, v_A$, where $v_A = 580$ km s^{-1} is the Alfvén speed for our choice of the parameters. It is to be noted that the amplitude v_0 is kept same as in S. Mondal et al. (2024a). This pulse is basically mimicking a large-scale EUV wave often observed to be propagating in the large-scale corona after its transient generation during onset of solar flares and CMEs (e.g., R. Zheng et al. 2014; L. Li et al. 2018; R. Zheng et al. 2022).

We use open-source MPI-AMRVAC[1] (C. Xia et al. 2018; R. Keppens et al. 2023) to numerically solve the following resistive magnetohydrodynamic (MHD) equations in their conservative form (S. Sen & R. Keppens 2022; S. Sen et al. 2023; S. Mondal et al. 2024b):

$$\frac{\partial \rho}{\partial t} + \nabla \cdot (\rho \boldsymbol{V}) = 0, \tag{5}$$

$$\frac{\partial}{\partial t}(\rho \boldsymbol{v}) + \nabla \cdot \left[\rho \boldsymbol{v}\boldsymbol{v} + p_{\rm tot}\boldsymbol{I} - \frac{\boldsymbol{B}\boldsymbol{B}}{4\pi}\right] = 0, \tag{6}$$

$$\frac{\partial e}{\partial t} + \nabla \cdot \left(e\boldsymbol{v} + p_{\rm tot}\boldsymbol{v} - \frac{\boldsymbol{B}\boldsymbol{B}}{4\pi} \cdot \boldsymbol{v}\right) = \eta \boldsymbol{J}^2 - \boldsymbol{B} \cdot \nabla \times (\eta \boldsymbol{J}) + \nabla_{\parallel} \cdot (\kappa_{\parallel} \nabla_{\parallel} T) - \rho^2 \Lambda(T), \tag{7}$$

$$\frac{\partial \boldsymbol{B}}{\partial t} + \nabla \cdot (\boldsymbol{v}\boldsymbol{B} - \boldsymbol{B}\boldsymbol{v}) + \nabla \times (\eta \boldsymbol{J}) = 0, \tag{8}$$

where

$$p_{\rm tot} = p + \frac{\boldsymbol{B}^2}{8\pi}, \quad e = \frac{p}{\gamma - 1} + \frac{1}{2}\rho v^2 + \frac{B^2}{8\pi}, \quad \boldsymbol{J} = \frac{\nabla \times \boldsymbol{B}}{4\pi}, \quad \nabla \cdot \boldsymbol{B} = 0. \tag{9}$$

Here, magnetic diffusivity η is taken to be 2.4×10^8 m^2 s^{-1} throughout the simulation domain, which corresponds to a Lundquist number of 4.8×10^5. It is to be noted that this diffusivity is kept same as in S. Mondal et al. (2024a). $\kappa_{\parallel} = 10^{-6} T^{5/2}$ erg cm^{-1} s^{-1} K^{-1} is the component of the TC tensor along the magnetic field. It is worth to mention that since solar corona is fully ionized and magnetically dominated, we do not consider the TC perpendicular to the magnetic field. But since, we are interested in formation and evolution of the plasmoids in the present work, presence of perpendicular TC may govern the formation and thermal characteristics of such fine structures (R. A. M. van der Linden & M. Goossens 1991). However, R. C. Ireland et al. (1992) suggested that the presence of finite resistivity results in similar effects as presence of perpendicular TC in formation and evolution of fine structures such as plasmoids etc. Therefore, absence of perpendicular TC will not change the characteristics of the reconnection dynamics and plasmoids in the presence of the finite resistivity. The optically thin RC depends on the local density, and the temperature-sensitive cooling models. In this work, we use the cooling model as reported by J. Colgan et al.(2008).

Since the abovementioned Equations (1)–(9) are solved numerically, all of the physical variables are made dimensionless using the corresponding factors as follows (X. Zhao et al. 2017; S. Mondal et al. 2024a): $L^* = 10^9$ cm, $\rho^* = 2.34 \times 10^{-15}$ g cm^{-3}, $V^* = 116.45$ km s^{-1}, $P^* = 0.32$ dyne cm^{-2}, $B^* = 2$ Gauss, $T^* = 1$ MK, and $J^* = 4.77$ statA cm^{-2}. The simulation domain spatially extends from -100 Mm to 100 Mm in the x-direction and 0 to 200 Mm in the y-direction. The physical total time duration of our simulation is 962 s (i.e., around 16 minutes). The initial coarse spatial resolution is 1.25 Mm in both the directions which reaches to highest resolution of 78 km after adaptive mesh refinement (AMR) of four levels. Temporal integration is carried out using "two-step" Runge–Kutta method. Estimation of the flux at cell interfaces is performed via "Harten Lax van Leer (HLL)" flux scheme (A. Harten 1983). All the physical variables are zero-order extrapolated using the closest inner mesh cell value to all of the ghost cells, i.e., the gradient is kept zero for all the variables across each boundary to ensure no reflection.

3. Results

We follow S. Mondal et al. (2024a) to initiate thinning of the CS due to inward pressure and density gradient, which results due to an interaction of velocity perturbation with the CS and its immediate surroundings (see Figure 1 and Section 3.1.1 of S. Mondal et al. 2024a for more details). However, contrary to S. Mondal et al. (2024a), we perturb the CS asymmetrically about its length. Even though the initial amplitude of velocity perturbation is taken to be $3V^*$, i.e., 350 km s^{-1} (see left panel of Figure 1), we find that the resultant amplitude of this perturbation

[1] http://amrvac.org

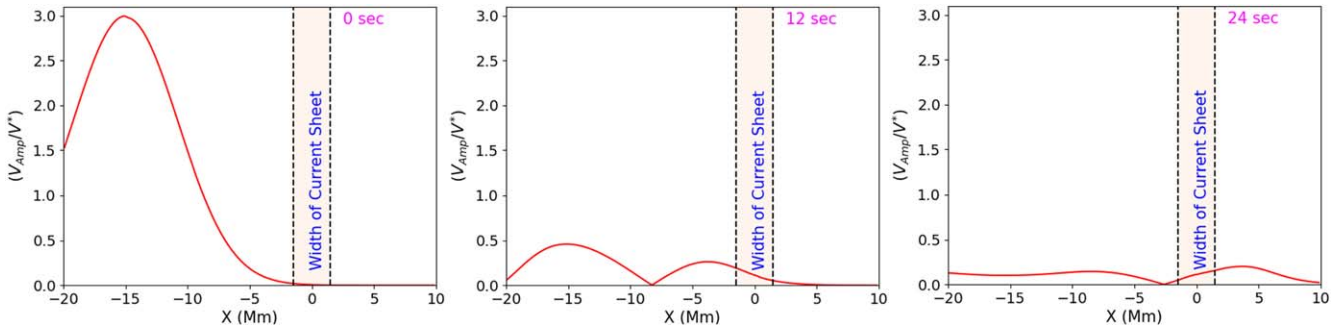

Figure 1. Temporal evolution of the initial velocity disturbance during its passage toward and through the CS as estimated at $y = 65$ Mm. At 0 s, the disturbance is properly Gaussian shaped centered at $x = -15$ Mm. As it propagates, it gets distorted and its amplitude becomes much smaller at the instance of interaction with the CS (12 s). The shaded region within vertical dashed black lines show the initial location and width of the CS in all the panels. At 24 s, the initial perturbation almost passed through the CS. It is to be noted that the velocity disturbance evolves exactly in similar manner with same amplitude before or even after its interaction with the CS in all four cases such as no energy loss (NEL), TC only, RC only, and TC+RC. Hence, we do not explicitly show those overlapping profiles in this figure.

is around $0.25V^*$, i.e., 30 km s^{-1} during its interaction with the CS (see middle panel of Figure 1). We do not find any sawtooth-like profiles as an indication of shock formation from this initial disturbances as in S. Mondal et al. (2024b). Rather they propagate as sinusoidal features such as waves in the present case. Since, the leading peak travels a distance of roughly 11 Mm in first 12 s, the estimated speed of the disturbance is around 915 km s^{-1}. Hence, the velocity disturbance works as a fast magnetosonic wave propagating across vertical field lines. In the present work, our main aim is to find out the differences in the entire dynamics due to presence of energy-loss effects in the form of field-aligned TC and RC. Hence, we will discuss the differences and/or similarities in the stage-wise dynamics and thermal characteristics for four different cases such as—(I) No energy loss (hereafter, NEL); (II) RC only; (III) TC only; and (IV) TC+RC. It is worth mentioning that the presence or absence of energy-loss effects such as TC and RC do not affect the evolution of the velocity perturbation before or even after its interaction with the CS. In addition, the perturbation in each plasma parameter such as density, temperature, etc. caused due to the velocity disturbance in all four cases do not differ from each other significantly. Therefore, we do not exhibit any explicit presentation of overlapping profiles of propagating time-evolved velocity disturbance or perturbation in plasma parameters in the abovementioned four cases in Figure 1. Since the velocity perturbation takes roughly 24 s only to traverse 15 Mm while reaching the CS in the homogeneous ambient corona, it does not get enough time to dissipate within the region of interest due to presence of energy-loss effects as this timescale is very less compared to the typical thermal conductive and RC timescales. However, the visually detectable differences in density and current density snapshots at 950 s for four different cases indicate that energy-loss effects may affect the dynamics in the time-evolving CS (see Figure 2 and associated animation). Hence, let us discuss in detail the morphological differences in the context of plasmoid formation and motion in aforementioned different cases.

3.1. Morphological Differences in Multiple Plasmoid Formation and Their Motions

(I) *NEL*. In the absence of any energy-loss effects, the plasmoid becomes visible for the first instance around 757 s which then grows a little bigger during its downward propagation. Another plasmoid forms around $y = 95$ Mm at 793 s and then propagates upward. At 830 s, a less pronounced plasmoid is formed around $y = 25$ Mm and is subjected to downward propagation. At around $y = 65$ Mm, one more plasmoid forms around 926 s which further moves downward along the CS.

(II) *RC only*. In the presence of RC only, the first plasmoid forms around 781 s at around $y = 65$ Mm and undergoes downward motion. Around 818 s, another plasmoid becomes visible around $y = 100$ Mm and starts propagating upward while it gets bigger in its dimensions. A very tiny plasmoid is found to move downward starting from around $y = 55$ Mm at 926 s.

(III) *TC only*. When a field-aligned TC is the only energy-loss effect present in our simulation, we found that the first plasmoid forms at $y = 75$ Mm around 721 s and then grows bigger in its voyage toward the upward direction. Two less prominent tiny plasmoids are formed around $y = 40$ Mm and $y = 90$ Mm at 914 s and 926 s respectively. These two plasmoids undergo downward and upward propagation respectively.

(IV) *TC+RC*. In the presence of both TC and RC, a plasmoid is detected for the first time at 757 s around $y = 50$ Mm and propagates downward with time and grows bigger in dimensions simultaneously. Around 842 s, less pronounced plasmoid forms close to upward propagating outward plasma and merge with the outflowing plasma instantaneously. No more plasmoids are seen to form within the CS.

All of these discussed morphological differences are evident in the animation associated with Figure 2. Therefore, even though the onset of CS dynamics has been carried out via the exact same prescription as proposed by S. Mondal et al. (2024a) except asymmetric interaction of velocity perturbation and the CS, the later phase dynamics within the CS is different in all four cases. Animation roughly indicates that the dynamics within the CS may evolve in a similar manner for aforementioned four cases up to around 600 s, i.e., before fragmentation of the CS. However, we will first discuss about the thinning and elongation of the CS in all the cases until 600 s as quantitative measures to closely examine the similarities or differences in CS dynamics before focusing on plasmoid formation and its subsequent motions. It is to be noted that we do not consider first 228 s while undertaking any quantitative estimations to ensure that the initial velocity pulse (which perturbs the force-free CS) has completely left the simulation domain without any reflections from all boundaries.

3.2. Temporal Variation of CS Dimensions before Onset of Fragmentation

Up to 600 s, CS does not undergo to a visibly detectable fragmentation and further a plasmoid formation stage in any

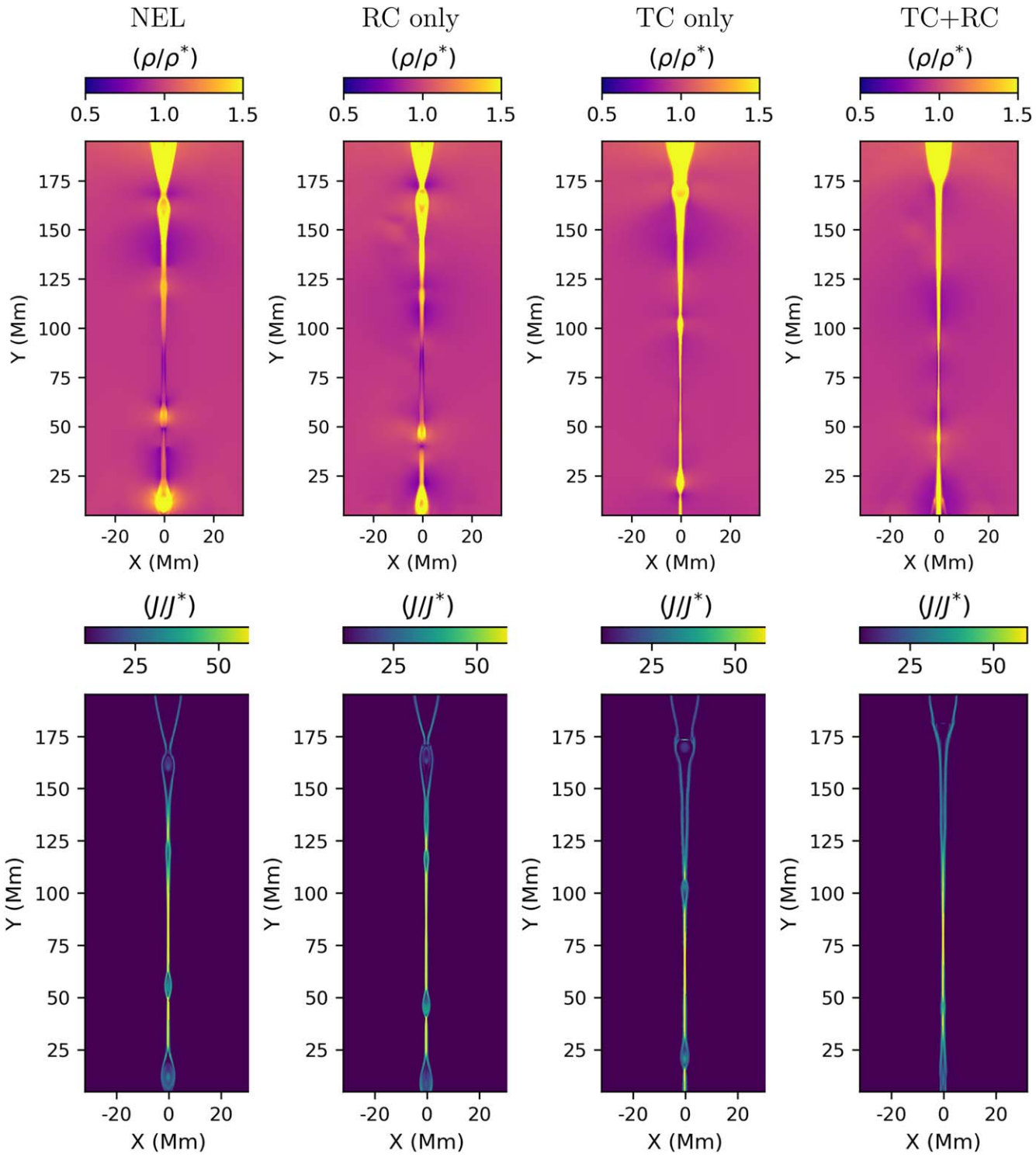

Figure 2. Top: spatial density distribution within the tearing mode unstable CS and its immediate surroundings at 950 s in the absence of energy-loss effects (denoted as NEL), presence of RC, presence of TC, and presence of TC+RC (left to right). Bottom: spatial distribution of current density there at 950 s for the aforementioned four cases. An animated version of the entire dynamics from 240 s to 962 s is available. The real time duration of the animation is 6 s. The triggering and initial evolution of the CS is similar to S. Mondal et al. (2024a) except the point of initial interaction being at $y = 65$ Mm instead of $y = 100$ Mm, i.e., asymmetric about its length. Hence, we do not present snapshots from 0 to 228 s explicitly.

(An animation of this figure is available in the online article.)

of the considered cases. Therefore, we estimate width and length of the CS as a full width half maximum (FWHM) of Gaussian functions fitted on the current density distribution across the CS at $y = 65$ Mm, and along the CS at $x = 0$ Mm respectively. Basically we use (S. Mondal et al. 2024a)

$$G(s, \sigma) = C \quad \exp\left(\frac{-(s - \bar{S})^2}{2\sigma^2}\right), \tag{10}$$

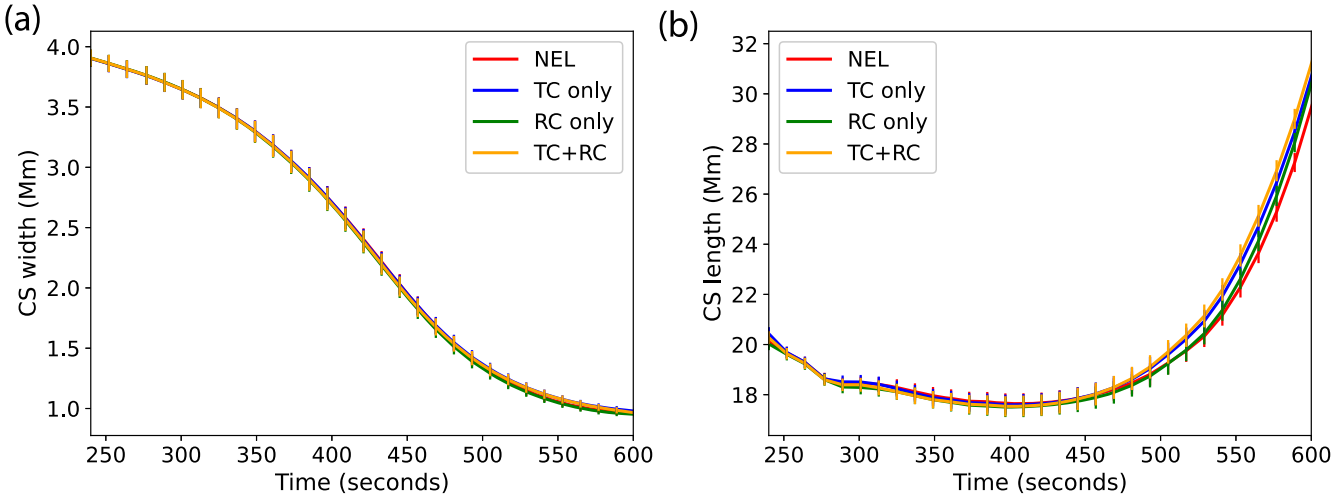

Figure 3. Panels (a) and (b) exhibit variation of CS widths and CS lengths with time from 240 to 600 s. The error bars are plotted after multiplied by a factor of 2 for better visualization. Panel (a) exhibits that there are no differences between CS widths throughout the considered time window for all the four cases studied. The minimal visible distinctions in CS length profiles after around 500 s are not significant enough to be attributed to presence of energy-loss effects in the thinning phase.

where s can either be x or y for estimation of CS width or length, respectively. C is the maximum of the current density which is also the peak of the Gaussian function. $\bar{S}$ is the x or y coordinates of the Gaussian peak during estimation of width or length respectively. The estimated value of σ is then used to obtain FWHM of the distribution as

$$\mathrm{FWHM} = 2\sqrt{2\sigma^2\, ln2}\,. \tag{11}$$

We find that the estimated widths of the CS are decreasing at similar rates and similar manner for aforementioned four cases (see panel (a) of Figure 3). Therefore, we infer that the thinning of the CS entirely depends on the external perturbation and is independent of the presence or absence of cooling effects. On the other hand, initially the lengths of the effective diffusion region along the CS slightly decreased from 240 to 420 s (see panel (b) of Figure 3). Thereafter, the CS lengths are found to increase at a faster rate after around 420 s which may be a signature of onset of magnetic reconnection (see panel (b) in Figure 3). There seem to be differences in the measured CS lengths once we reach close to 600 s (see panel (b) in Figure 3) However, close inspection suggests that current density profiles along the CS start to deviate slightly from Gaussian profile after around 540 s due to its gradual flattening. This results in an additional systematic error along with random error associated with Gaussian fitting. Error bars in both panel of Figure 3 stand only for random errors associated with Gaussian fitting and do not consider systematic error due to flattening of the current density profile. Since, flattening and deviation from the Gaussian profile will vary with time in all the cases, therefore increasing differences in estimated CS lengths can also be within the total uncertainties of the measurements. Therefore, even though estimated FWHMs in the time window 540–600 s give an indication of how the CS lengths are changing with time, they are not completely reliable for drawing any important physical interpretation about the presence of energy-loss effects on the basis of differences in CS length in different cases. Therefore, slight deviations are not considered as significant enough to correlate with presence of energy-loss effects in the presence of case-specific time-varying systematic errors. In addition, as discussed in Sections 3.8 and 3.9, there is no distinction in rate of decrease in average magnetic energy density and increase of average kinetic energy density in the time window of interest, i.e., 480–600 s for different four cases which further suggests that energy redistribution due to presence of energy-loss effects are not effective in this time window. Therefore, we conclude that energy-loss effects do not play any significant role in CS dynamics until 600 s, i.e., in the thinning and elongation phase of the externally perturbed CS. Now, let us shift our focus to the onset times of fragmentation and deduce the Lundquist number and aspect ratio as two indicators of the onset of tearing within the CS at those times.

3.3. Estimation of Instantaneous Lundquist Number and Aspect Ratio at Onset Time of Fragmentation of the CS

As discussed in the previous section, we fit the current density profiles along and across the CS with Gaussian functions to find out the length and width of the CS until 600 s. But after 540 s itself, the current density profiles become flatter along the CS so that they cannot be fitted properly using Gaussian function. However, the peak of current density along and across the CS should be closely consistent with each other, i.e., the difference is less than and not close to 1 until there is onset of fragmentation of the CS. Hence, we choose to set a criterion that the time when those two peaks are differing from each other by more than 1 in normalized units will be taken as the onset time of fragmentation. In addition, since, we cannot rely anymore on FWHM extracted from Gaussian fitting to deduce CS length, we rather find out the distances along CS at which the current density becomes half of the instantaneous maximum. We consider the difference between pair of such distances as the length of the CS. In addition, we find out the average Alfvén speeds in between those pair of distances. In this way, we find that in the case without energy loss, fragmentation starts at 661 s with estimated CS length being 50.79 Mm. The instantaneous average Alfvén speed is found to be 310 $\mathrm{km\,s^{-1}}$. Therefore, the Lundquist number is equal to 6.56×10^4 at the onset of fragmentation or tearing along the CS in the absence of any energy-loss effects. When only TC is

present as an energy-loss effect, fragmentation starts around 625 s within a CS of 39.53 Mm length. The average Alfvén speed is found to be 359 km s^{-1}. Hence, the estimated Lundquist number is 5.91×10^4. However, fragmentation starts later at 685 s when only RC is present. In that case, the CS length and average Alfvén speed are estimated to be 62.19 Mm and 291 km s^{-1} which corresponds to a value of 7.54×10^4 of the Lundquist number. In a similar way, we find that when both TC and RC are taken into account, the onset of fragmentation takes place around 661 s within a CS having 51.42 Mm length. The average Alfvén speed is found to be 319 km s^{-1}. This corresponds to a Lundquist number of 6.8×10^4. The corresponding aspect ratio of the CS are 51, 41, 61, and 56 for the NEL case, TC only, RC only, and TC +RC respectively. It has been found that the aspect ratio of the CS should be equal or higher than $S_L^{1/3}$ for the development of ideal tearing instability, where S_L stands for the Lundquist number (K. Shibata & S. Tanuma 2001; F. Pucci & M. Velli 2014; A. Tenerani et al. 2016). Here, estimated aspect ratios and instantaneous Lundquist numbers in all four cases validate such a criterion. If we consider aspect ratio is equal to S_L^{α} (A. Bhattacharjee et al. 2009), we find α to be 0.35, 0.34, 0.37, and 0.36 for the NEL case, TC only, RC only, and TC+RC respectively, which are close to but slightly higher than 1/3. Therefore, the comparison of values of the Lundquist number, aspect ratio, as well as onset times of fragmentation possibly suggests that the presence of TC is advancing the onset of tearing process, whereas the presence of RC has the opposite effect. We further estimate growth rates of linear tearing instability using (A. Bhattacharjee et al. 2009)

$$\gamma_{L,\max} = S_L^{(3\alpha-1)/2} \times v_A/L \tag{12}$$

at the onset time of tearing with L and v_A being the instantaneous CS length and average Alfvén speed as mentioned above. The estimated growth rates are 8.1×10^{-3} s^{-1}, 10^{-2} s^{-1}, 8.7×10^{-3} s^{-1}, and 9.6×10^{-3} s^{-1} for without energy-loss effects, TC only, RC only, and TC +RC which correspond to 125 s, 100 s, 114 s, and 104 s as times required for growth of primary plasmoids in those cases respectively. Therefore, the presence of TC certainly enhances the growth rate of tearing mode after its onset. Now the times of onset of fragmentations are roughly 96 s before the first instances of visibility of primary plasmoid in all four cases as far as crude visual inspections are concerned. Therefore, the theoretically calculated time required for growth of the tearing mode is consistent with the approximate time gap between onset of fragmentation and the first visible inspection of plasmoids. Hence, a different Lundquist number and aspect ratio required for plasmoid formation suggest that the presence of energy-loss effect certainly starts to affect the CS dynamics once it advances toward tearing instability. Therefore, let us see how the rate of reconnection is getting affected due to presence of such effects in next section.

3.4. Temporal Variation of Reconnection Rate from 240 to 962 s

To understand reconnection dynamics, one important way is to measure reconnection rate. We find out the maximum of current density, i.e., $J_{\max}$ along the CS and use $\eta J_{\max}$ as the measure of reconnection rate following T. Yokoyama & K. Shibata (2001) and S. Mondal et al. (2024a). $\eta J_{\max}$ basically gives the resistive component of electric field in Ohm's law. From Figure 4, it seems that reconnection rate is varying in a similar way for all cases up to 600 s without any detectable differences. After 600 s, reconnection rate keeps on increasing in the presence of TC only and TC+RC before reaching peaks at 721 s and 757 s respectively. These times are consistent with the instances when the first plasmoids become visible in these two cases (see blue and orange dashed vertical lines in Figure 4). However, the rate profiles are subjected to the formation of plateaus or nearly constant values in the absence of any energy-loss mechanism (i.e., NEL case) and RC-only case before peaking at 757 s and 781 s respectively during the first visualization of their primary plasmoids. After achieving the first peak, the reconnection rate exhibits distinct oscillatory behavior at a later stage that is associated to the collective outcome of different plasmoid dynamics in those cases. It is evident that the presence of TC enhances the reconnection rate, i.e., results in a faster reconnection after onset of tearing instability. However, in tearing unstable CS, reconnection takes place with a slower rate in the presence of RC only than that in case without any energy-loss effects. When both the effects are at work, the resultant reconnection rate is faster than that in the case without energy loss and closer to the profile for the TC-only case. This suggests that energy loss may be taking place mostly through TC even when both TC and RC are present in our system since TC and RC have opposite effects individually. Since the presence of energy-loss effects are affecting the rate of reconnection, we then focus on finding out dynamical and thermal properties of the plasmoids and reconnection outflows in all four cases as discussed in the following section.

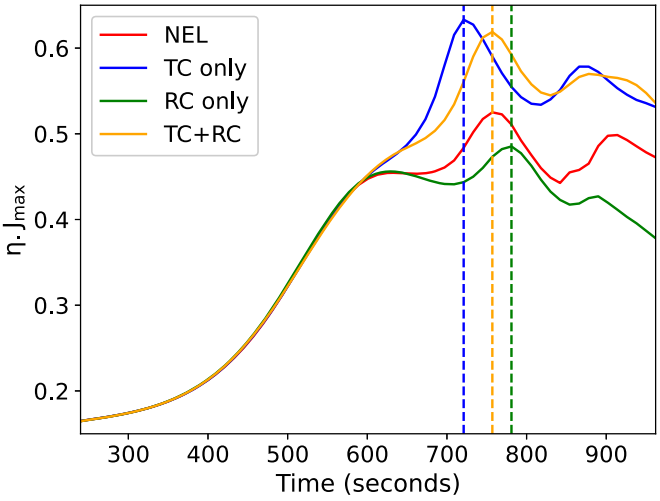

Figure 4. Temporal variation of estimated reconnection rate using $\eta J_{\max}$ during the period of 240 s to 962 s i.e., up to the end of simulation. The figure gives an indication that the reconnection rate profiles in all the cases are overlapping with each other up to 600 s. After 600 s, reconnection rates keep on increasing before attaining first peak for the cases TC only and TC+RC. On the other hand, for cases without energy loss and RC only, reconnection rates become almost constant or decrease slightly before finally subjected to increment just before reaching the first peaks. Blue, orange, and green dashed vertical lines denote the times at which primary plasmoids become visible in case with TC only, TC+RC, and RC only. Red dashed line is overlapping with the orange one.

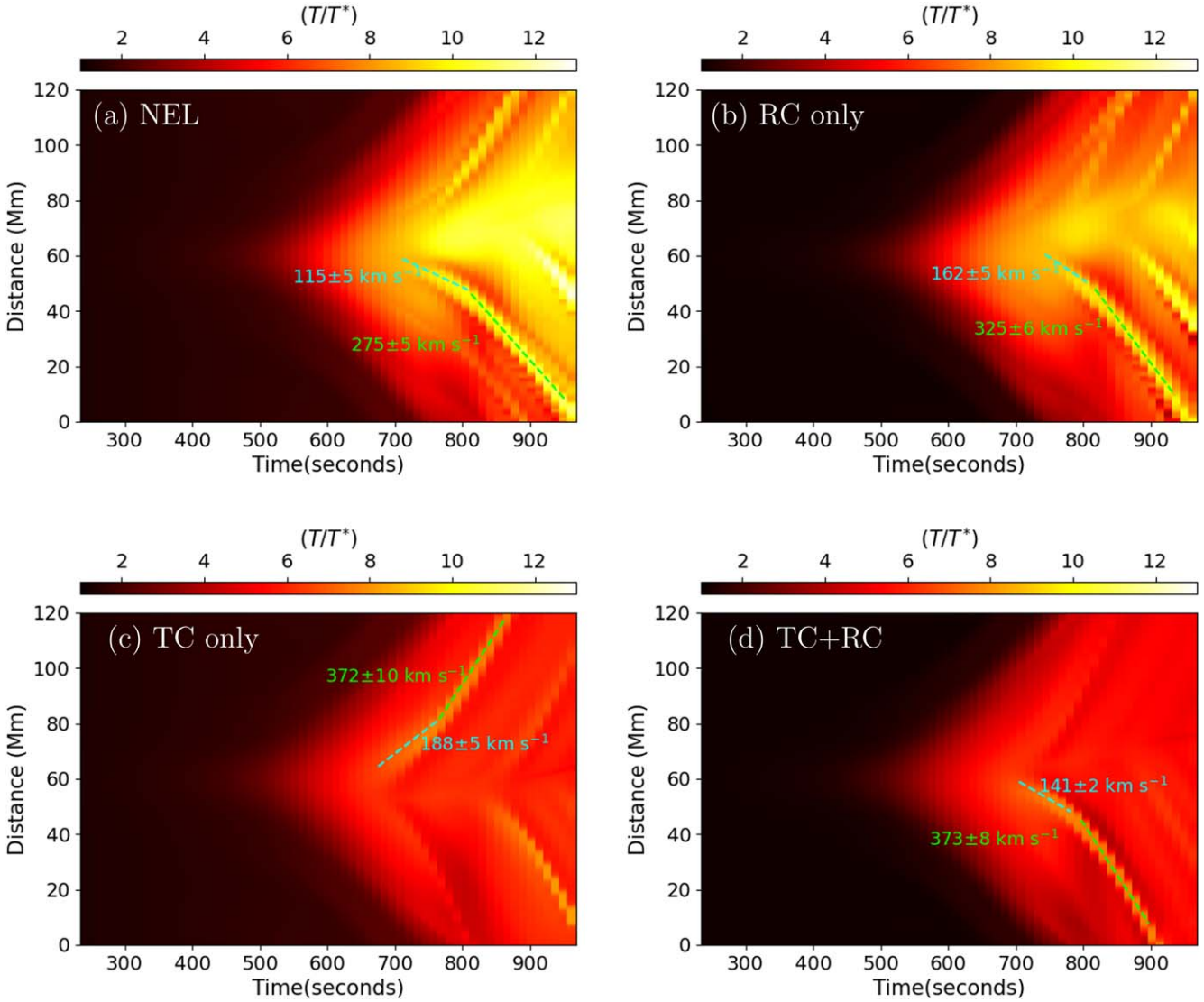

Figure 5. Reconnection outflows, plasmoid dynamics and its thermal properties are shown for no energy loss (NEL; panel (a)), only RC (panel (b)), only TC (panel (c)), and both in the presence of RC+TC (panel (d)). Spatiotemporal variation of temperature along the CS is derived along $x = 0$ Mm from $y = 5$ Mm to $y = 125$ Mm. The start and end points of the slit are taken to be symmetrically placed with respect to 65 Mm, i.e., the location at which the initial Gaussian pulse interacts with the CS first. The accelerated motion of plasmoids are also evident from broken fitted straight lines (cyan- and lime-dashed lines). It is to be noted that distances exhibited in the y-axis in all four panels are distances measured from $y = 5$ Mm, i.e., 0 Mm in y-axis corresponds to $y = 5$ Mm.

3.5. Comparison of Distribution of Temperature and Velocities of Outward-moving Plasmoids along CS

TC transports heat from hotter to cooler parts of a system via the collisions of constituents of the system itself. On the other hand, RC heavily depends on density of the emitter. Hence, it will be interesting to examine how the temperature varies along the CS with time in the presence of such energy-loss mechanisms. Since TC transports heat via transfer of energy due to collisions of the vibrating constituents, the presence of TC also results in higher speed of bulk reconnection outflows to transport energy with a faster rate. To check whether these physical intuitions are correct or not, we quantify time-distance diagrams in temperature to investigate the spatiotemporal variation in temperature along the CS between $y = 5$ Mm and $y = 125$ Mm to maintain symmetry about primary interaction region, i.e., $y = 65$ Mm, which also provide evidence of reconnection outflows and the propagation of multiple plasmoids along the CS. We find that there is hardly any difference in the starting time of reconnection outflows (around 480–500 s) in all four cases under consideration. Figure 5(a) exhibits higher temperature in regions between distances of 60 Mm and 80 Mm, i.e., $y = 65$ Mm to $y = 85$ Mm and relatively lower temperature at the outer portions of the CS in the absence of any energy-loss mechanisms. In the presence of RC only, the temperature seems to be reduced slightly in the aforementioned middle portion of the CS compared to the NEL case (See Figure 5(b)). However, in the presence of TC or TC +RC, there are no such relatively higher temperature regions visible along the CS (see panels (c) and (d) of Figure 5). Possibly, TC is dominantly redistributing the energy along the field lines in the outflowing plasma, so it appears more uniform in temperature without any high-temperature plasma strands as seen in Figures 5(a) and (b). The time-distance diagrams also exhibit differences in the number of visible plasmoids and their motions, i.e., whether they are moving upward or downward. These notions are consistent with the morphological differences described in Section 3.1. Since we find clear evidence of

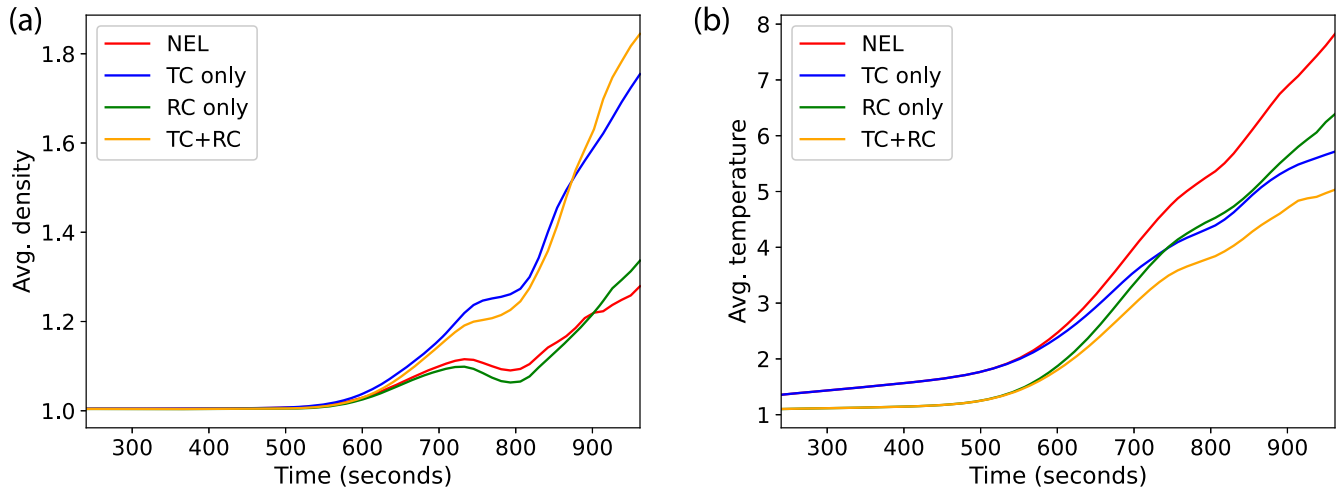

Figure 6. Panel (a) exhibits the variation of average density along the CS with time in dimensionless forms for all four cases. Panel (b) shows the same for temperature. The average has been done within $x = [-1\ \mathrm{Mm}, 1\ \mathrm{Mm}]$ and $y = [0, 200\ \mathrm{Mm}]$.

outward plasmoid motions along the CS, we further aim to find out the velocities of plasmoids. We find acceleration profiles for outward-moving plasmoids in all the cases. In the absence of any energy-loss mechanisms, plasmoids are found to have velocity around $115 \pm 5\ \mathrm{km\ s^{-1}}$ near to the distance of 60 Mm (hereafter, the central region of the CS) which then reaches to $275 \pm 5\ \mathrm{km\ s^{-1}}$ during its downward propagation (see Figure 5(a)). In the presence of RC only, the velocity of the plasmoid increases to $325 \pm 6\ \mathrm{km\ s^{-1}}$ at outer portion from $162 \pm 5\ \mathrm{km\ s^{-1}}$ in the central region (See panel (b) of Figure 5). In case of TC only and TC+RC, the velocity of the plasmoid increases to $372 \pm 10\ \mathrm{km\ s^{-1}}$ and $373 \pm 8\ \mathrm{km\ s^{-1}}$ from $188 \pm 5\ \mathrm{km\ s^{-1}}$ and $141 \pm 2\ \mathrm{km\ s^{-1}}$ respectively (see panels (c) and (d) of Figure 5). One standard deviation of the measured slopes via straight line fitting is considered as uncertainties of measurements here. Notable increases in the velocities of plasmoids in the presence of TC and TC+RC relative to those in the absence of any energy-loss effect confirm the positive effect of those effects on dynamics within tearing unstable CS at later phases in the magnetic reconnection. Actually in the presence of TC and TC+RC, reconnection occurs at a higher rate once the CS undergoes fragmentation (see Figure 4). Therefore, speed of the reconnection outflows will be higher which further push the plasmoids more to move outward, resulting in its higher speed in the presence of TC and TC+RC. Now we will discuss the average behavior of physical quantities like density and temperature, along with magnetic and kinetic counterparts of energy densities within the reconnecting CS.

3.6. Temporal Variation of Average Density from 240 to 962 s

Density is one important physical quantity of any plasma systems which controls the intensity of radiation emitted from such systems at specific temperatures. Therefore, a knowledge of average density will be a ready reference to understand how much intense the modeled reconnecting CS should be in observational perspective. In addition, it will provide a rough idea about the filling factor of high dense plasma within the CS in comparison to the background corona. Since the dynamics along the CS is kinematically and thermally different in four cases, we perform averaging of physical quantities along the CS to find out the effect of presence or absence of energy-loss effects on the energetics associated with the dynamic CS undergoing to a tearing instability and plasmoid formation. Since reconnection outflow starts around 480–500 s (see all panels of Figure 5) and CS width becomes less than 2 Mm after 450 s (see Figure 3(a)), we have to consider the x extents of the domain used for averaging in such a way that it will cover the entire width of the CS without taking significant contribution from the background in the neighborhood of the CS. Therefore, we perform the averaging of the physical parameters within $x = [-1\ \mathrm{Mm}, 1\ \mathrm{Mm}]$ and $y = [0, 200\ \mathrm{Mm}]$. From Figure 6(a), it is evident that average density within the aforementioned domain varies similarly for all the four cases roughly until 588–600 s. After 600 s, there is clear distinction between the estimated average densities for different cases. Average density increases at higher rates in the presence of TC only and TC +RC. It reaches 1.75 and 1.84 times the initial value for TC only and TC+RC respectively at the end of the simulation (see Figure 6(a)). Since there are less prominent plasmoid formations after the primary stage and therefore less secondary fragmentations, the average density keeps on increasing in these two cases. However, in the absence of energy-loss effects or in the presence of RC only, multiple stages of plasmoid formations are present which may create voids of densities in its vicinity which then results in lower values on averaging even in the presence of highly dense plasma blobs. Hence, the average densities are subjected to less increment rate in case of NEL and RC only and reach around 1.27 and 1.33 times of the initial value respectively by the end of the simulation (see Figure 6(a)).

3.7. Temporal Variation of Average Temperature from 240 to 962 s

Even though from Figure 5, we obtain an approximate idea about the distribution of the temperature along the CS, it will be important to see how the average temperature is evolving with time within the CS to understand the role of energy-loss effects on the rate of rise of temperature of the CS as a collective system. Further, it will provide important information about the potential contribution of such reconnection in coronal heating in localized solar corona in the presence of energy-loss effects. Therefore, we extract the average temperature within the spatial domain denoted in Section 3.6. It is found that average

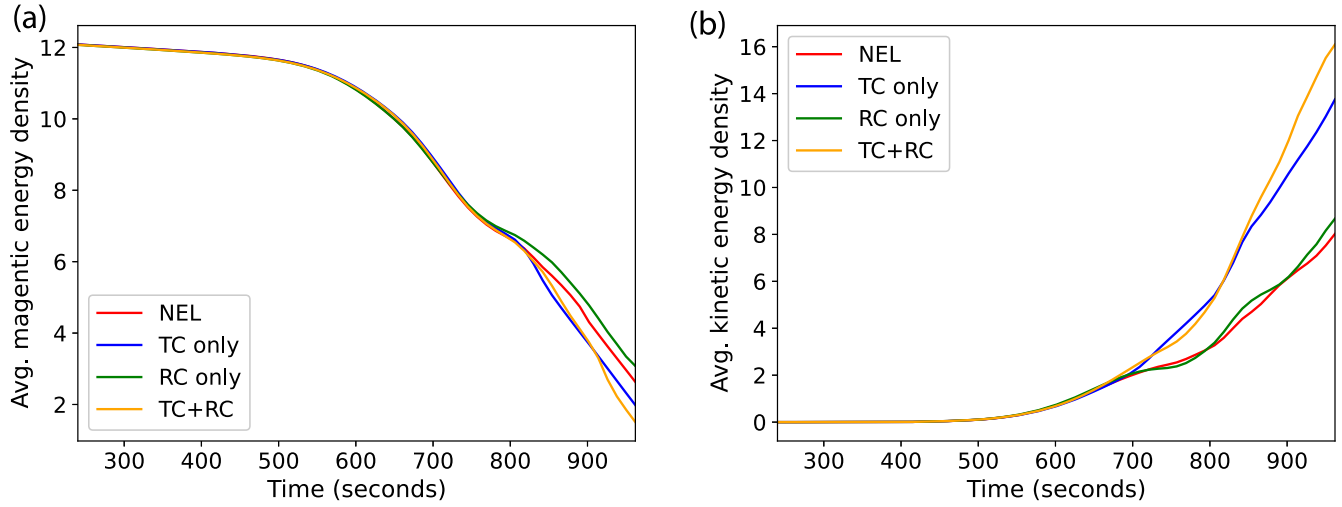

Figure 7. Panel (a) exhibits the average magnetic energy density ($\frac{B^2}{2}$) with time for all four cases from 240 to 962 s. The averaging has been done within $x = [-1$ Mm, 1 Mm] and $y = [0, 200$ Mm]. Panel (b) shows variation of average kinetic energy density ($\frac{1}{2}\rho v^2$) with time from 240 to 962 s within the same domain along the CS. Both the quantities are shown in dimensionless form.

temperature keeps on increasing in all the cases (See Figure 6(b)). However, as expected, the presence of energy-loss effects certainly decreases the rate of increase of temperature. But the resultant increase indicates that the heating rate must be higher than the corresponding energy-loss rates. Nevertheless, the average temperature increases almost 7.8 times of its initial value in the absence of any energy-loss effects. However, average temperature increases up to 5 times of its initial value when both TC and RC are present as energy-loss mechanisms (See Figure 6(b)). Interestingly, a clear distinction is found in temperature profiles from 240 s itself. Actually, it is evident that the presence of RC and TC +RC results in similar average temperature within the CS up to around 588–600 s (see Figure 6(b)). However, the presence of TC hardly has any effect until 588–600 s as evident from an overlap of temperature profiles without energy loss or with TC only. This scenario indicate that RC is effective even before the fragmentation of the CS due to enhancement in density in outflow regions. However, TC comes into play after 600 s. A possible reason behind the increased effectiveness of TC might be the temperature gradients resulted during fragmentation of the CS which further increases during and after plasmoid formations. However, since there is no prominent secondary fragmentations, the gradients in temperature will not remain high enough for continuous energy loss via TC. Therefore, the average temperature increases up to around 5.7 times in the presence of TC only by the end of the simulation. However, the RC rate decreases after 600 s as a collective effect of less increment in density and temperature-dependent cooling function. Therefore, the temperature increases around 6.4 times of its initial value at the end of the simulation in the presence of RC only (see Figure 6(b)).

3.8. Temporal Variation of Average Magnetic Energy Density from 240 to 962 s

In magnetic reconnection, stored magnetic energy gets transformed into other forms of energy such as thermal energy, bulk kinetic energy, etc. Hence, it is interesting to see how the presence of energy-loss effects affect the rate of decrease of stored magnetic energy within the reconnecting CS and further compare it with rate of reconnection as discussed in Section 3.4. Therefore, we calculate the average magnetic energy density ($\frac{B^2}{2}$) within the same spatial domain as mentioned in Section 3.6. The variation of estimated average magnetic energy with time suggests that the decrements are taking place at a very slow rate until 500 s. After 500 s, the rate of decrement becomes faster which is a signature of onset of magnetic reconnection. As expected, the rates are found to be similar in all the four cases until around 700 s (see Figure 7(a)). Within 600–700 s, the rate is even faster than before which suggests onset of fragmentation of the CS. Hence, magnetic energy starts to be diminished at a higher rate when the CS undergoes fragmentation. After around 720–733 s, the rates of decrement of the average magnetic energy density become distinct in all four cases. In the presence of TC and TC+RC, magnetic energy decreases at a faster rate (see blue and orange curves in Figure 7(a)) which is consistent with higher reconnection rate in those cases as discussed in Section 3.4. However, the rate of decrement of magnetic energy becomes slightly slower in case without energy loss and RC only. This is also consistent with reconnection rates for these two cases as shown in Figure 4 and discussed in Section 3.4.

3.9. Temporal Variation of Average Kinetic Energy Density from 240 to 962 s

Since magnetic reconnection results in generation of kinetic energy of the plasma embedded within the reconnecting CS, we wish to investigate the differences in the rate of increase in kinetic energy with time in all four cases to understand how the energetic outcome of reconnection gets modified due to presence of energy-loss effects. In addition, since kinetic energy will only become nonzero after onset of reconnection outflows, it will further provide confirmation of the onset time of reconnection. Hence, estimation of average kinetic energy density ($\frac{1}{2}\rho v^2$) is carried out within same spatial domain. Estimated average kinetic energy densities are found to be nearly zero until 500 s (see Figure 7(b)). This is consistent with the facts that magnetic energies hardly undergo any decrement until 500 s (see Figure 7(a)) and reconnection outflows start around 500 s as shown in Figure 5. From 500 s to 720–733 s

roughly, the estimated kinetic energy increases with similar rate in all four cases. This is consistent with similar decrement rates of magnetic energy densities in this time window (as described in the previous section). After that, the rate of increment of kinetic energy density becomes higher in the presence of TC only and TC+RC (see blue and orange curves in Figure 7(b)). However, in the absence of any energy-loss effect and in the presence of RC only, kinetic energy density seems to increase with a slightly lower rate with time (see red and green curves in Figure 7(b)). These higher values of estimated average kinetic energy density in the presence of TC only and TC+RC are consistent with the calculated higher speeds of plasmoids in those cases as discussed in Section 3.5.

4. Discussion and Conclusion

In this work, we aim to model an externally driven magnetic reconnection in an elongated coronal CS in the absence of any localized enhancement of resistivity due to increase in current density. Following S. Mondal et al. (2024a), we perturb the CS via an external Gaussian velocity pulse. Since both EUV waves and CSs are ubiquitous in the solar corona, it is important to study such kind of interaction. Since such an interaction results in the onset of magnetic reconnection in the present case, we consider it as one feature of the Symbiosis of WAves and Reconnection (SWAR; S. Mondal et al. 2024b; A. K. Srivastava et al. 2024). Basically, here, the system is in magnetohydrostatic equilibrium and does not undergo any dynamics if it is not subjected to wave-like perturbation. Hence, here, the onset of reconnection is fully attributed to interaction of wave-like perturbation with the CS. Hence, this simulated event qualifies as one example of SWAR.

In the present case, velocity pulse is propagating anisotropically, i.e., the standard deviation in x-direction is higher than that in y-direction. Unlike S. Mondal et al. (2024a), pulse also initially interacts with the CS at an off-centered location along its length. These initial considerations provide a more general modeled scenario of nonsymmetric interaction between CS and anisotropically propagating Gaussian pulse akin of EUV waves in solar corona. In addition, since both TC and radiative loss are important in solar coronal conditions, it is of utmost importance to include them while studying any magnetoplasma processes such as magnetic reconnection and associated physical conditions in solar corona. Therefore, we also consider such energy-loss effects in this present work to examine how they affect various stages of the reconnection dynamics and associated energetics both individually and compositely. Here we summarize the important scientific findings as follows.

(i) Before onset of fragmentation, until about 600 s, thinning and elongation of the perturbed CS are nearly independent of the presence or absence of energy-loss effects.

(ii) For all the cases, estimated values of the local Lundquist number, i.e., S_L, just at the onset of fragmentation are certainly higher than the previously reported lower threshold of 3×10^4 as deduced by A. Bhattacharjee et al. (2009) in their simulation. However, estimated Lundquist numbers are almost 2 times their reported value. Now, the criterion of aspect ratio being higher than $S_L^{1/3}$ is more important for the onset of tearing mode instability. Therefore, higher values of the Lundquist number are possibly needed to satisfy this criterion for our present simulated dynamics with specific rate of thinning, elongation of the CS, decrement in magnetic energy controlled via our choice of magnetic diffusivity, and inflows induced via interaction of velocity perturbation and the CS.

(iii) Relative comparison of onset time of fragmentation, Lundquist number, and aspect ratio suggest that TC advances the onset of the primary tearing process, whereas the presence of RC delays the onset of tearing. We find that the times of the first visible detections of plasmoid in all the cases are 96 s after the respective onset times of fragmentation in those cases.

(iv) Reconnection is taking place at similar rates in all four cases before the start of fragmentation. But once the CS fragments to form plasmoids subsequently, the presence of TC and TC+RC result in faster reconnection than in the other two cases.

(v) Reconnection outflows and plasmoids undergo acceleration in propagation speeds during their outward motion along the CS. Plasmoids finally attain much higher velocity when the energy-loss effects are present than in their absence.

(vi) Presence of TC and TC+RC result in more uniform temperature distribution along the CS than in the other two cases. This suggests that TC is the dominant mechanism of energy loss in the solar coronal condition.

(vii) In tearing unstable CS, the average density increases with higher rate in the presence of TC and TC+RC than in the other two cases. This confirms more uniform distribution of dense plasma along the CS in those cases.

(viii) As expected, average temperature increases with respectively highest and lowest rate in the absence of any energy-loss effects and in the presence of both TC and RC simultaneously.

(ix) When the CS is undergoing tearing and plasmoid formation, the average magnetic energy density decreases with higher rates in the presence of TC and TC+RC than in the other two cases. This is consistent with faster reconnection rate in the presence of TC and TC+RC in tearing unstable CS.

(x) In tearing unstable CS, average kinetic energy density increases with considerably higher rates when TC and TC+RC are present. However, the rates of the same remains less in the case without energy loss and in the presence of RC only.

S. Mondal et al. (2024a) showed that the reconnection dynamics took place as per considered physical magnetic diffusivity instead of being controlled by numerical diffusivity. In their simulation, the smallest grid size was 97.5 km. Since, in the present work, the smallest grid size is 78 km, the simulated dynamics is certainly physical instead of being governed by numerical diffusivity. In S. Mondal et al. (2024a), the reconnection rate was found to be less than 0.45. But here, the rate even reaches more than 0.6 in the presence of the TC. Even in the NEL case in the present work, the rate is reaching around 0.52, contrary to 0.45 in S. Mondal et al. (2024a). In S. Mondal et al. (2024a), the reconnection rate is subjected to a less oscillatory nature followed by a steep decrease of its value. They have described the presence of monster plasmoid at the center of the CS as the reason behind that particular physical scenario. In this present case, oscillatory profiles are more prominent, and these rate profiles do not suffer any steep decrement at later times. This feature is consistent with the absence of any steady monster plasmoid.

S. Sen & R. Keppens (2022) reported that tearing can take place even at a Lundquist number smaller than 3×10^4 when the system is subjected to thermal imbalance between RC and time-independent background heating. Here, we do not have any constant background heating term, rather we rely on ohmic

heating only to counterbalance RC. We notice that in the present case, presence of RC is delaying the onset of tearing process via requirement of higher Lundquist number and higher aspect ratio. But the growth rate of linear tearing mode after the onset of fragmentation increases slightly in the presence of RC in comparison to that in the absence of energy-loss effects. Basically, S. Sen & R. Keppens (2022) reported that tearing can be initiated at a lower Lundquist number in the presence of RC than in the absence of energy-loss mechanisms. On the other hand, we find that a higher Lundquist number is required for the onset of fragmentation in the presence of RC in our study. However, enhancement of the growth rate of tearing mode after its onset in the presence of RC in comparison to that in the absence of energy-loss effects in the present study supports the findings of S. Sen & R. Keppens (2022). S. Sen & R. Keppens (2022) used magnetic field perturbation to perturb the CS throughout its length simultaneously in the absence of any guide field. However, we used wave-like perturbation primarily interacting with the CS at certain location in the presence of guide magnetic field. We observe only a few plasmoids instead of having a bead-like feature formed by plasmoid chain along the CS (S. Sen & R. Keppens 2022). Hence, we do not have a large number of highly dense plasma blobs as in S. Sen & R. Keppens (2022), which may result in less effectiveness of radiative loss in our simulation.

S. Sen et al. (2023) studied thermally coupled tearing in a 3D initially force-free coronal CS in the presence of background heating, radiative loss, and field-aligned TC. They reported that TC is only trying to homogenize temperature along the CS. Contrary to S. Sen & R. Keppens (2022), they found that the CS undergoes a pure tearing instability initially, resulting in 3D topological changes in the magnetic field to form magnetic flux ropes, and only thereafter exhibits runaway condensations near the central portion of the CS. Even though we do not have a signature of the thermal runaway process in our present simulation, it will be worthwhile to extend the current study to 3D in the future to examine the role of energy-loss effects in the formation and evolution of flux ropes in a 3D setup and make several scientific comparisons since we find that TC is playing a more important role in the present simulated reconnection dynamics than that in S. Sen et al. (2023) and will transport thermal energy or heat additionally along the guide fields associated with the flux ropes. We will undertake such a study in the near future.

Finally, we conclude that the externally driven reconnection dynamics strongly depend on the nature of external perturbation, its interaction point along the CS. Depending on the nature of perturbation, the CS undergoes different types of tearing instability, i.e., primary tearing sets at once either in the entire CS to form a chain of small plasmoids or in some specific parts of the CS to generate fewer plasmoids. In addition, the presence of a guide field may suppress tearing of the CS. The mode of tearing instability results in the diverse nature of the temperature gradient and the dense plasma distribution along the CS. Hence, the nature of external perturbation and the presence of guide field control how TC and RC will affect the reconnection dynamics. In the present work, we only consider the external forcing aspect to initiate reconnection in the presence of uniform resistivity independent of current density and time. Consideration of such an enhancement in resistivity might affect the entire reconnection dynamics in terms of how much faster it will be. However, whether it will alter the effect of the presence of energy-loss effects will be interesting to explore in future work. Now, longer CSs with a higher Lundquist number are more prone to tearing, such as in the solar corona. But in other plasma systems, such as the solar chromosphere and laboratory scales, the Lundquist number will not be as high as in the corona. Therefore, it will be interesting to see whether similar wave-like perturbation can lead to plasmoid formation there. Moreover, the role of TC and radiative loss on externally driven reconnection dynamics and associated energetics in those magnetoplasma systems will be explored in detail in future works.

Acknowledgments

We are grateful to the anonymous reviewer for constructive suggestions, which helped us to improve the manuscript scientifically. We sincerely thank Prof. Eric R. Priest for fruitful primary discussions. We are thankful for open-source MPI-AMRVAC 3.0, which provides a user-friendly framework to develop new routines required to simulate our scientific idea. S.M. acknowledges the financial support provided by the Prime Minister's Research Fellowship (PMRF) of India. A.K.S. would like to acknowledge the ISRO grant (DS/2B-13012(2)/26/2022-Sec.2) for the support of his scientific research.

Software: MPI-AMRVAC, Python.

ORCID iDs

Sripan Mondal https://orcid.org/0009-0000-3578-8270
A. K. Srivastava https://orcid.org/0000-0002-1641-1539

References

Baty, H., Forbes, T. G., & Priest, E. R. 2009, PhPl, 16, 012102
Bhattacharjee, A., Huang, Y.-M., Yang, H., et al. 2009, PhPl, 16, 112102
Chae, J., Cho, K., Kwon, R.-Y., et al. 2017, ApJ, 841, 49
Cheng, X., Li, Y., Wan, L. F., et al. 2018, ApJ, 866, 64
Colgan, J., Abdallah, J., & Sherrill, M. E. 2008, ApJ, 689, 585
Comisso, L., Lingam, M., Huang, Y.-M., et al. 2017, ApJ, 850, 142
Ding, T., & Zhang, J. 2024, ApJ, 974, 104
Færder, Ø. H., Nóbrega-Siverio, D., & Carlsson, M. 2024, A&A, 683, A95
Fárnìk, F., Kaastra, J., Kálmán, B., et al. 1983, SoPh, 89, 355
French, R. J., Matthews, S. A., Jonathan Rae, I., et al. 2021, ApJ, 922, 117
French, R. J., Matthews, S. A., van Driel-Gesztelyi, L., et al. 2020, ApJ, 900, 192
Guo, L.-J., Bhattacharjee, A., & Huang, Y.-M. 2013, ApJL, 771, L14
Harten, A. 1983, JCoPh, 49, 357
Huang, Y.-M., & Bhattacharjee, A. 2010, PhPl, 17, 062104
Huang, Y.-M., & Bhattacharjee, A. 2016, ApJ, 818, 20
Ireland, R. C., van der Linden, R. A. M., Hood, A. W., et al. 1992, SoPh, 142, 265
Keppens, R., Popescu Braileanu, B., Zhou, Y., et al. 2023, A&A, 673, A66
Kropotina, J. A., Webster, L., Artemyev, A. V., et al. 2021, ApJ, 913, 142
Kumar, P., Nakariakov, V. M., Karpen, J. T., et al. 2024, NatCo, 15, 2667
Kwon, R.-Y., Vourlidas, A., & Webb, D. 2016, ApJ, 826, 94
Ledentsov, L. 2021a, SoPh, 296, 74
Ledentsov, L. 2021b, SoPh, 296, 93
Lemen, J. R., Title, A. M., Akin, D. J., et al. 2012, SoPh, 275, 17
Li, L., Zhang, J., Peter, H., et al. 2018, ApJL, 868, L33
Li, Y., Xue, J. C., Ding, M. D., et al. 2018, ApJL, 853, L15
Liu, R., Lee, J., Wang, T., et al. 2010, ApJL, 723, L28
Liu, W., & Ofman, L. 2014, SoPh, 289, 3233
Long, D. M., Bloomfield, D. S., Chen, P. F., et al. 2017, SoPh, 292, 7
Loureiro, N. F., Schekochihin, A. A., & Cowley, S. C. 2007, PhPl, 14, 100703
Mann, G., & Veronig, A. M. 2023, A&A, 676, A144
Maynard, N. C., Burke, W. J., Ober, D. M., et al. 2007, JGRA, 112, A12219
Mondal, S., Srivastava, A. K., Pontin, D. I., et al. 2024a, ApJ, 963, 139
Mondal, S., Srivastava, A. K., Pontin, D. I., et al. 2024b, ApJ, 977, 235
Muhr, N., Veronig, A. M., Kienreich, I. W., et al. 2014, SoPh, 289, 4563
Nitta, N. V., Schrijver, C. J., Title, A. M., et al. 2013, ApJ, 776, 58

Odstrcil, D., & Karlicky, M. 1997, AdSpR, 19, 1895
Patel, R., Pant, V., Chandrashekhar, K., et al. 2020, A&A, 644, A158
Pontin, D. I., & Priest, E. R. 2022, LRSP, 19, 1
Priest, E. 2014, Magnetohydrodynamics of the Sun, 2014 (Cambridge: Cambridge Univ. Press)
Pucci, F., & Velli, M. 2014, ApJL, 780, L19
Riley, P., Lionello, R., Mikić, Z., et al. 2007, ApJ, 655, 591
Sakai, J., Tajima, T., & Brunel, F. 1984, SoPh, 91, 103
Sen, S., Jenkins, J., & Keppens, R. 2023, A&A, 678, A132
Sen, S., & Keppens, R. 2022, A&A, 666, A28
Shen, Y., Liu, Y., Liu, Y. D., et al. 2018, ApJ, 861, 105
Shibata, K., & Tanuma, S. 2001, EP&S, 53, 473
Shimizu, T., & Kondoh, K. 2022, arXiv:2209.00149
Srivastava, A. K., Mishra, S. K., & Jelìnek, P. 2021, ApJ, 920, 18
Srivastava, A. K., Mishra, S. K., Jelìnek, P., et al. 2019, ApJ, 887, 137
Srivastava, A. K., Priest, E. R., Ofman, L., et al. 2024, in COSPAR 45th Scientific Assembly, E2.7–0002–24
Svestka, Z. 1981, Solar Flare Magnetohydrodynamics (New York, NY: Gordon and Breach Science Publishers), 47
Tenerani, A., Velli, M., Pucci, F., et al. 2016, JPlPh, 82, 535820501
Treumann, R. A., & Baumjohann, W. 2015, A&ARv, 23, 4
van der Linden, R. A. M., & Goossens, M. 1991, SoPh, 134, 247
Vanninathan, K., Veronig, A. M., Dissauer, K., et al. 2015, ApJ, 812, 173
Vekstein, G. 2017, JPlPh, 83, 205830501
Veronig, A. M., Podladchikova, T., Dissauer, K., et al. 2018, ApJ, 868, 107
Wang, H., Chae, J., Yurchyshyn, V., et al. 2001, ApJ, 559, 1171
Xia, C., Teunissen, J., El Mellah, I., et al. 2018, ApJS, 234, 30
Yang, L., Yan, X., Xue, Z., et al. 2024, MNRAS, 528, 1094
Yokoyama, T., & Shibata, K. 2001, ApJ, 549, 1160
Zhang, Q. M., Ji, H. S., & Su, Y. N. 2016, SoPh, 291, 859
Zhao, X., Xia, C., Keppens, R., et al. 2017, ApJ, 841, 106
Zheng, R., Jiang, Y., Yang, J., et al. 2014, MNRAS, 444, 1119
Zheng, R., Wang, B., Zhang, L., et al. 2022, ApJL, 929, L4
Zhou, G., Gao, G., Wang, J., et al. 2020, ApJ, 905, 150